LIDAR MEASUREMENTS OF THE ATMOSPHERIC ENTRAINMENT ZONE AND THE POTENTIAL TEMPERATURE JUMP ACROSS THE TOP OF THE MIXED LAYER

R. BOERS

Laboratory for Atmospheres
NASA/Goddard Space Flight Center, Code 611/615.2, Greenbelt, MD 20771, U.S.A.

and

E. W. ELORANTA

Department of Meteorology, Madison, WI 53706, U.S.A.

(Received in final form 15 July, 1985)

Abstract. Lidar measurements of the thickness of the atmospheric entrainment zone are presented. The measurements were obtained in central Illinois during 6 days of clear-air convection.

A new method was developed to monitor the potential temperature jump across the entrainment zone. A single early morning temperature sounding and continuous lidar measurements of the mixed-layer height provide potential temperature jump values which agree well with in situ observations.

Lidar measurements of the thickness of the entrainment zone normalized by mixed-layer depth are presented as a function of a 'convective' Richardson number; these values show reasonable agreement with published laboratory results. The lidar observations span a wider range of mixed-layer depths and contain higher values of the normalized entrainment rate $(dh/dt)/w_*$ than those observed in tank studies. Both lidar and tank results show that simple parcel theory does not properly predict entrainment-zone thickness. During this experiment which examined mostly high entrainment conditions, the normalized entrainment-layer thickness was linearly dependent on entrainment rate.

1. Introduction

In laboratory and atmospheric studies of the convectively mixed layer, it is commonly observed that the top of the mixed layer has an irregular structure (Kunkel *et al.*, 1977; Deardorff *et al.*, 1969; Deardorff *et al.*, 1980; Raymond and Readings, 1974; Hardy and Ottersten, 1969; Konrad, 1970; and others). These irregular structures are caused by heated parcels of mixed-layer air overshooting the interface with the stable outer fluid. In between the domes that are created in this fashion, stable fluid is entrained into the mixed layer at the expense of turbulence energy generated within the mixed layer. Various investigators (Zeman and Tennekes, 1977; Phillips, 1972; Mahrt, 1979; Stull, 1973; Deardorff *et al.*, 1980; Deardorff, 1979) have tried to parameterize the depth of the overshoot distance in terms of the mixed-layer convective velocity scale and the buoyancy jump across the top of the mixed layer. These theories have been tested in a laboratory tank experiment by Deardorff *et al.* (1980). However, atmospheric data have been scarce. The requirement for measurements of the potential temperature jump to use in parameterization schemes has proven to be a major obstacle to verifying models with atmospheric data.

The importance of the overshoot distance as a second mixed-layer length scale was

Boundary-Layer Meteorology **34** (1986) 357–375.

recognized by Zeman and Tennekes (1977) who assumed that the energy dissipation at the top of the mixed layer scaled on the overshoot distance. Deardorff (1979) developed a mixed-layer model that explicitly takes this distance into account as a transition layer between the mixed layer and the stable air. In this transition layer, temperature, humidity, and wind varied smoothly from the values inside the mixed layer to their values in the stable atmosphere.

In this paper, we present lidar data of the atmospheric entrainment zone, viz., six case studies of clear air convection collected during the *C*entral *I*llinois *R*ainfall *C*hemistry *E*xperiments (CIRCE) in July 1979. We compare our observations with existing laboratory observations and with predictions based on parcel theory. For this purpose, we developed a method to determine the potential temperature jump across the top of the mixed layer based on only one temperature sounding and continuous lidar measurements of the mixed-layer height.

2. Depth of the Entrainment Zone

We adopt the entrainment zone definition of Deardorff *et al.* (1980): 'the depth being confined between the outermost height reached by only the most vigorous penetrating parcels, and by the lesser height where mixed-layer fluid occupies usually some 90 to 95% of the total area'. Deardorff *et al.* (1980) show that these heights determined visually from a laboratory experiment, appeared to be related to the outermost height where the horizontally averaged potential temperature flux and its vertical derivative vanished and the height where the potential temperature flux changed from a positive value inside the well mixed layer to a negative value in the layer above it where entrainment takes place. A typical temperature profile is illustrated in Figure 1.

A simple theoretical estimate of the depth of the entrainment zone can be obtained by assuming that a mixed-layer parcel traveling upward into the stable air loses its kinetic energy while gaining potential energy. If the kinetic energy of the parcel is proportional to the convective velocity w_*, the depth of the entrainment zone can be written as:

$$\Delta h = C \frac{T_0 w_*^2}{g \Delta \theta} \tag{1}$$

where

$\Delta\theta$ is the potential temperature jump across the entrainment zone
Δh is the depth of the entrainment zone
g is the gravitational constant
T_0 is a bulk temperature
c is a constant of proportionality
w_* is the convective velocity scale defined as

$$w_*^3 = \frac{g}{T_0} (\overline{\theta' w'})_s h \tag{2}$$

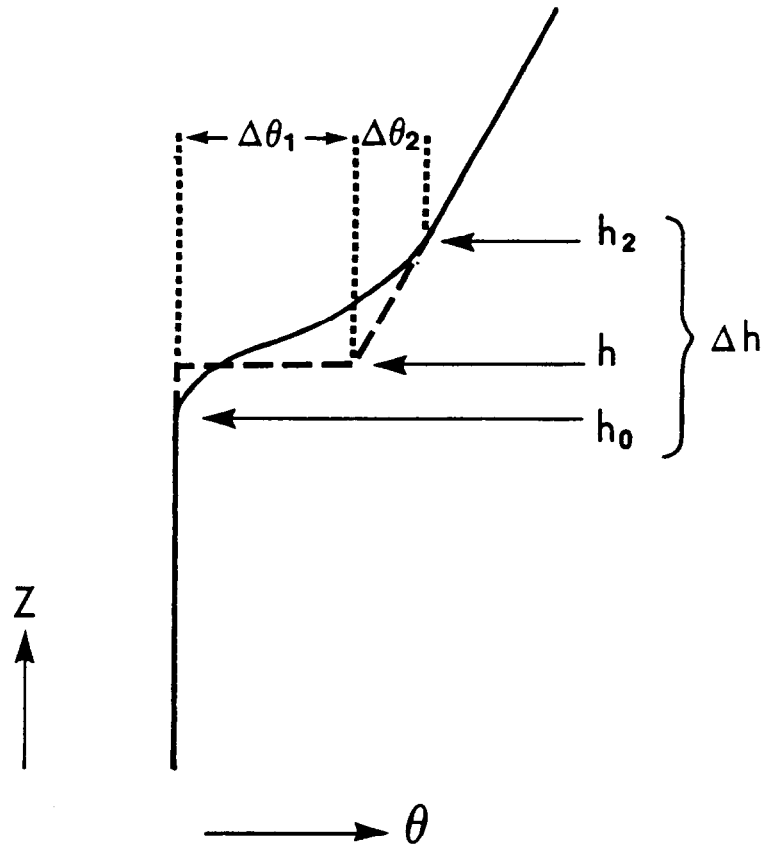

Fig. 1. Potential temperature as a function of height. Solid line represents the horizontally averaged potential temperature. The total potential temperature jump between the bottom (h_0) and top (h_2) of the entrainment zone is split into parts $\Delta\theta_1$ and $\Delta\theta_2$ as indicated by the thick broken line.

where

$(\overline{\theta' w'})_s$ the virtual potential temperature flux

h the mixed layer height.

This parameterization by Stull (1973) was used by Zeman and Tennekes (1977) as an estimate of a dissipation length scale at the mixed-layer top. Mahrt (1979) examined the details of the penetrative motions by defining three idealized stages of penetration each characterized by different time scales. He considered the effects of entrainment and pressure forces on an overshooting parcel. It was shown, however, that if the penetrative motion is primarily controlled by buoyancy effects, (1) should be valid.

Stull (1973) proposed an equation whereby the entrainment rate was proportional to the overshoot distance and inversely proportional to a time scale for the creation of a penetrative element at the top of the mixed layer:

$$\frac{\Delta h}{t_*} = \alpha\left(\frac{\mathrm{d}h}{\mathrm{d}t} - \overline{w}\right) \tag{3}$$

where α is constant, t_* is a time scale for the penetrative elements and $\overline{w}$ is the mean vertical velocity at the inversion base.

For a convective boundary layer with $t_* = h/w_*$, (3) can be written as:

$$\frac{\Delta h}{h} = \alpha \frac{1}{w_*} \left(\frac{\mathrm{d}h}{\mathrm{d}t} - \overline{w} \right). \tag{4}$$

3. Analysis

During CIRCE, the University of Wisconsin Lidar system was located close to Weldon in De Witt county in central Illinois (see Sroga *et al.*, 1980, for a description of the lidar instrument). To obtain data on the structure of convective plumes, the lidar was scanned in elevation angle while leaving the azimuth angle fixed (*R*ange *H*eight *I*ndicator, RHI-scan). With a pulse rate of 1 Hz, it takes one minute to complete a scan from the surface to an elevation of 60°. With a convective time scale typically of the order of 10 min, an essentially instantaneous cross-section of the mixed layer is obtained. The mixed layer is visualized by displaying relative backscatter intensity levels of lidar shot returns on a color-enhanced video system.

The lidar measurements were supplemented by surface measurements of sensible and latent heat flux and friction velocity, and pilot balloon and kytoon measurements of wind

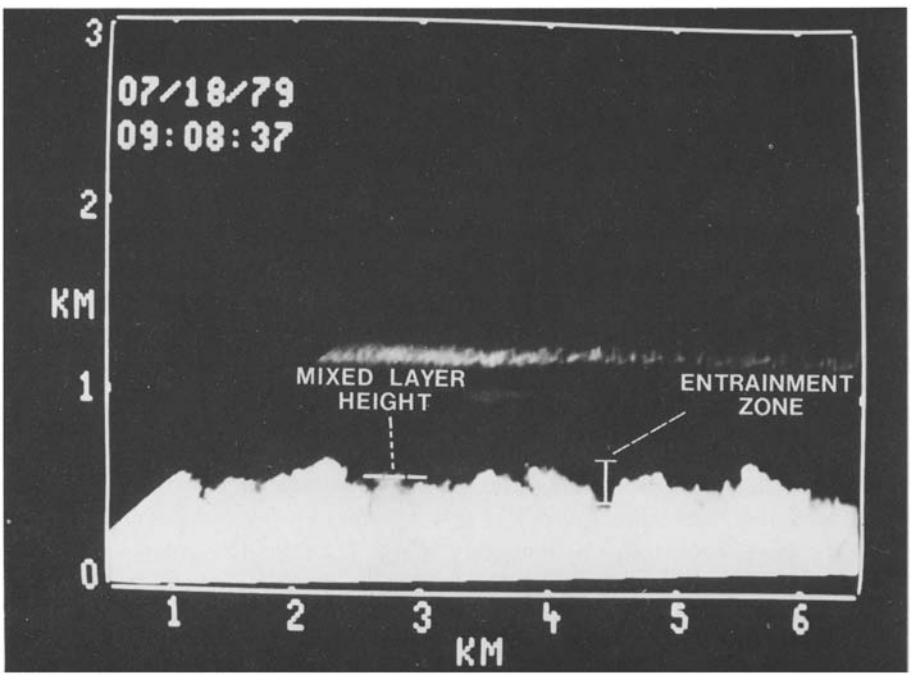

Fig. 2. Lidar RHI-picture taken on July 18, 1979 9:08 CST. White area is the mixed layer. Mean mixed-layer depth and entrainment zone are indicated on picture.

speed and temperature made by an Argonne National Laboratory Research team located (1.9 km northwest of the lidar site. The outer edge of the mixed layer was identified as a function of horizontal distance by observing the backscatter intensity difference between mixed-layer air and a continuous background level of clear-air backscatter. More contrast prevailed at the top of a protruding dome than at its side where clear air was entrained downward. The tops of the highest plumes could thus readily be identified. More care had to be taken in the determination of the mean mixed-layer height. This involved the identification of the level at which 50% of the horizontal area was covered by the clear-air background intensity level and the lower edge of the entrainment zone where the background level covered 10% of the area. Figure 2 shows a typical RHI-picture. The mean mixed-layer depth and entrainment zone are indicated in the picture.

Because of the subjective nature of the procedure, it was repeated some weeks after all the days had been analyzed to reduce visual errors to a minimum. Differences with earlier estimates were found to be less than 25 m in most cases. Measurements obtained from each group of 2 to 4 RHI-scans were averaged to increase the statistical significance. The procedure to obtain lidar measurements during the CIRCE-experiment is explained in detail by Boers *et al.* (1984).

Figure 3 shows measurements of the entrainment zone on the 18th of July 1979. The

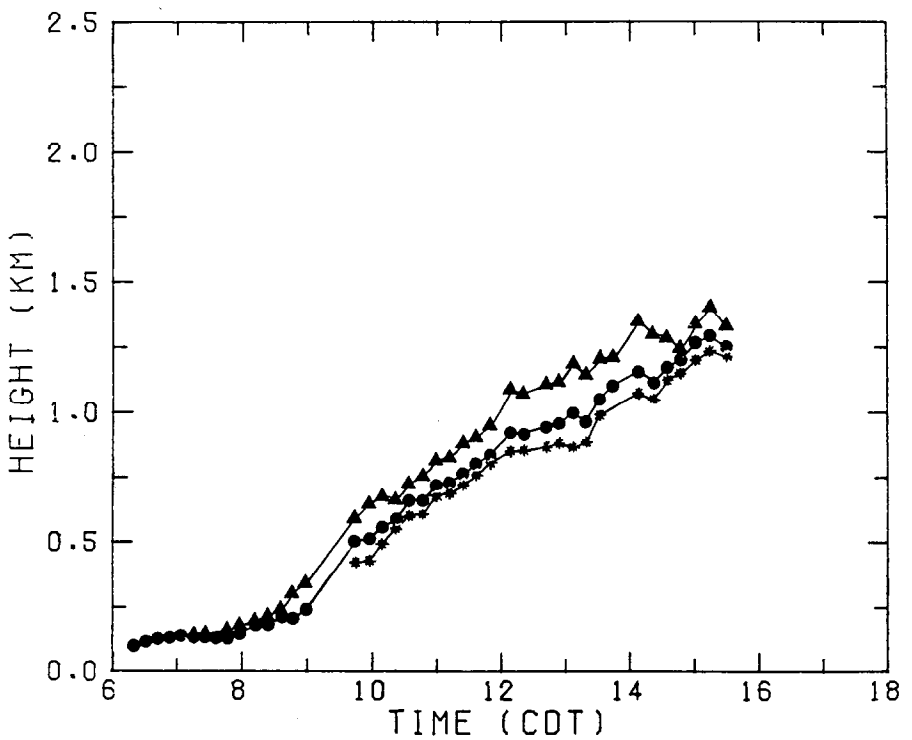

Fig. 3. Lidar measurements of the entrainment zone for July 18, 1979. (△) – the upper edge of the entrainment zone; (○) – the average mixed-layer height; (*) – the lower edge of the entrainment zone.

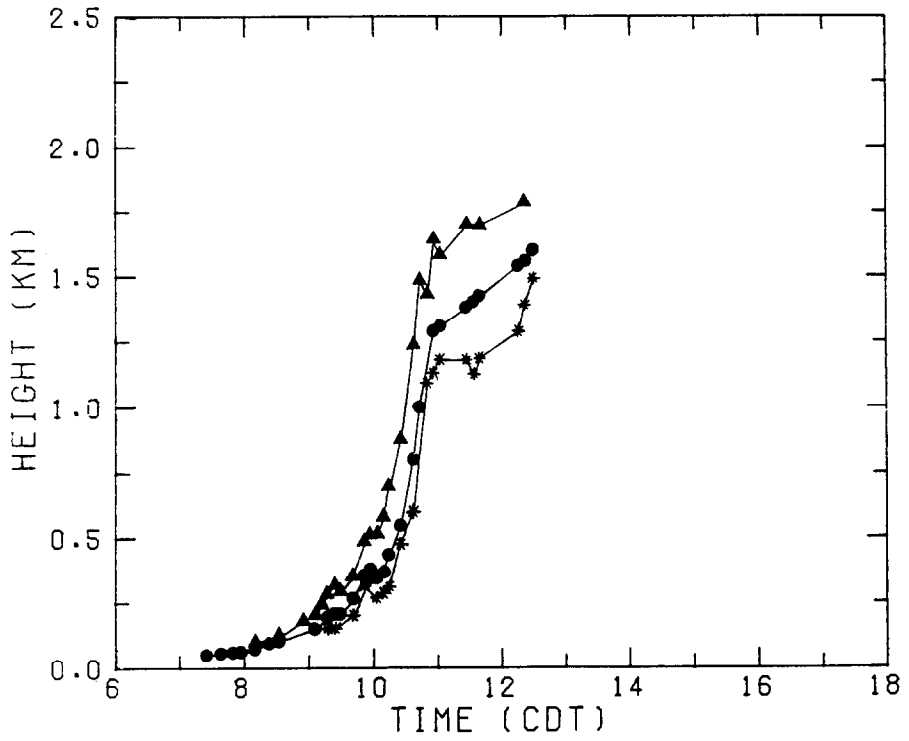

Fig. 4. As figure 3 for July 21, 1979.

mixed layer was rising at an almost constant rate into an environment with a stable lapse rate of 0.005 °C m^{-1}. The thickness of the entrainment zone shows only small variations as a function of time. Figure 4 shows the measurements for July 21st, 1979. Early morning measurements indicate that the entrainment zone is initially thin. The period of rapid entrainment around 1000 CDT, when the mixed layer grew into an almost neutral environment, is characterized by large plumes, similar to those observed by Kunkel *et al.* (1977). Around 1015 CDT cumulus clouds appeared. For the purpose of testing predictions, we omitted all measurements at times when clouds were present.

We consider again the profile shown in Figure 1. The total potential temperature jump $\Delta\theta$ can be expressed as:

$$\Delta\theta = \Delta\theta_1 + \Delta\theta_2 = \Delta\theta_1 + \gamma(h_2 - h) \tag{5}$$

where h_2 is the upper edge of the entrainment zone and γ is the lapse rate of potential temperature above the level h_2. The rate of change of $\Delta\theta_1$ is governed by the growth rate and heating of the mixed layer:

$$\frac{\mathrm{d}\Delta\theta_1}{\mathrm{d}t} = \gamma\left(\frac{\mathrm{d}h}{\mathrm{d}t} - \overline{w}\right) - \left[(\overline{\theta' w'})_s + \Delta\theta_1\left(\frac{\mathrm{d}h}{\mathrm{d}t} - \overline{w}\right)\right]\Big/ h$$

(See Tennekes, 1973) (6)

Strictly speaking, $\Delta\theta$ should be replaced by the virtual potential temperature jump $\Delta\theta_v$. However, during the experimental periods, no humidity profiles were measured except occasionally in the lowest 300 m. Therefore, observations of $\Delta\theta$ could not be corrected for moisture effects except when the boundary layer was very shallow. The few available observations of the humidity jumps showed that it was very small, indicating that the moisture correction to $\Delta\theta$ was negligible.

Similarly, the virtual potential temperature flux needs to be used instead of the potential temperature flux. Since moisture fluxes were available, the moisture corrections to the potential temperature flux were computed. The corrections were found to be substantial (30% to 50% of the potential temperature fluxes).

We assume for the moment that $\overline{w} = 0$. Equation (6) was solved using a temperature sounding to obtain $\Delta\theta_1$, and γ at the initial time, and a time record of the virtual potential temperature flux. The lidar-derived height measurements were fitted with a smoothing spline to obtain continuous measurements of the mixed-layer rise rate. This process is described in more detail by Boers *et al.* (1984). The solution to (6) was obtained using a numerical procedure similar to that used for a computational run of a zero-order jump model as discussed e.g., by Tennekes (1973) and Stull (1976). Since both h and $\Delta\theta_1$ are unknown in such models, an assumption for the downward buoyancy flux is needed for closure. In the present treatment, h is known and no closure is needed to obtain $\Delta\theta_1$.

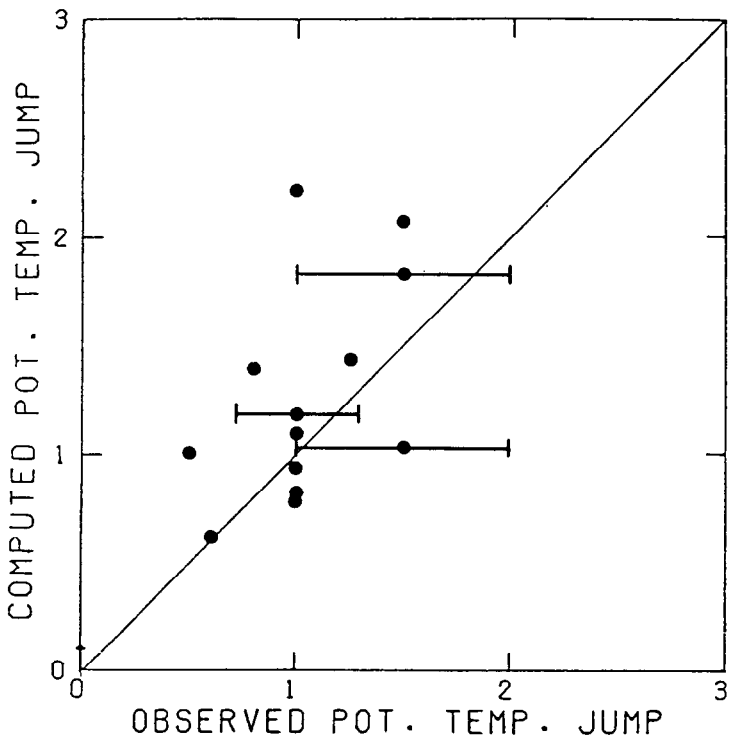

Fig. 5a. $\Delta\theta_1$ as measured from pilot balloon soundings (horizontal axis) versus $\Delta\theta_1$ as calculated from lidar data and Equation 6 (vertical axis). Representative error bars are indicated for the balloon measurements.

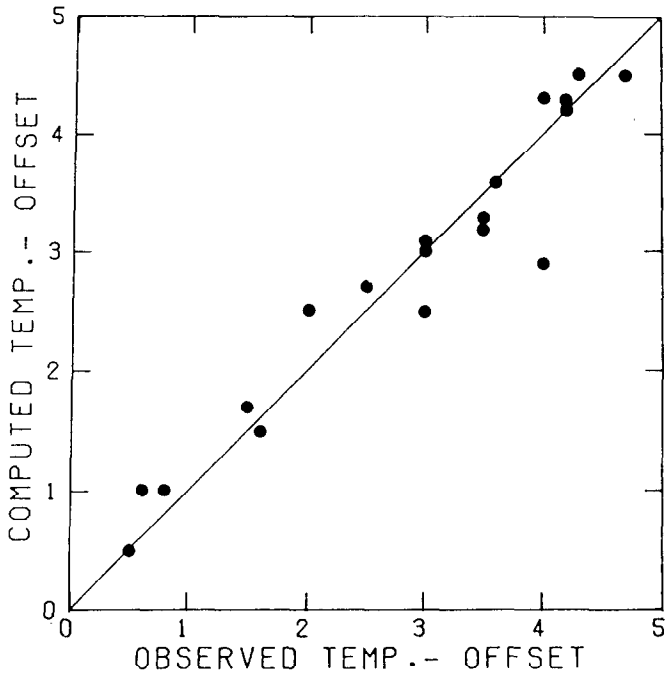

Fig. 5b. Calculated values of the (Potential temperature of mixed layer) – (Potential temperature at starting time of calculation) plotted on the vertical axis, versus kytoon measurements on the horizontal axis.

A comparison of these computed $\Delta\theta_1$ values with pilot balloon measurements is shown in Figure 5a. Agreement is fair. Note that measurements from soundings are very difficult to make since the magnitude of the temperature jump entirely depends on the transition point of the temperature-measuring device at the plume top. Errors indicated are for the visual estimates from the soundings. The effect of uncertainties in the sensible heat flux (10%) and latent heat flux (20%) on the $\Delta\theta_1$ calculations was found to be small. An independent check of our procedure is provided by a comparison of the mixed-layer potential temperature calculated by this procedure and measurements from kytoons. Figure 5b shows good agreement. No error bars are indicated since the kytoon measurement are very accurate (± 0.1 K).

The influence of surface divergence on the $\Delta\theta_1$ calculations was investigated by recomputing $\Delta\theta_1$, using values of $\overline{w}$ computed from the surface divergence. The surface divergence was computed from PAM-stations according to the procedure outlined by Boers *et al.* (1984). In all cases except the 19th, a positive divergence was present resulting in a downward motion at the top of the mixed layer, which decreased $\Delta\theta_1$ over time. The effect was most significant for the 17th and 18th. On the 17th, the fractional reduction in $\Delta\theta_1$ varied from 10% at 0900 CDT to 50% at 1300 DCT. On the 18th it varied between 5 and 15%.

In order to compute $\Delta\theta$, the second term on the right hand of Equation (5) involving the lapse rate had to be evaluated. A smoothing spline was fitted through the h_2

measurements. The difference in temperature at the levels h_2 and h could thus be derived from the mean potential temperature profiles.

$\Delta\theta_1$ and $\Delta\theta_2$ are listed in Table I in the Appendix as are the values for Ri, Ri_1, and Ri_2, where Ri, Ri_1, and Ri_2 are defined as

$$\mathrm{Ri} = \mathrm{Ri}_1 + \mathrm{Ri}_2 = \frac{g}{T_0}\frac{\Delta\theta_1 h}{w_*^2} + \frac{g}{T_0}\frac{\Delta\theta_2 h}{w_*^2} = \frac{g}{T_0}\frac{\Delta\theta h}{w_*^2}. \tag{7}$$

The column labeled Ri_D in Table I gives values of the convective Richardson number computed from Equation (7) with non-zero values of $\overline{w}$ used in the calculation of $\Delta\theta$.

4. Results

Inspection of Table I reveals that the contribution of $\Delta\theta_2$ of $\Delta\theta$ is frequently of the order of 30 to 50%. It shows that for parameterizations of Δh in zero-order jump models, both the lapse rate and the potential temperature jump need to be taken into account. Also, a diurnal cycle is visible in the Ri-data. In early morning, when the heat flux is small and $\Delta\theta$ large, Ri is large. In midmorning, as the layer warms, the temperature jump decreases and the surface virtual potential temperature flux increases, resulting in a reduction of Ri. Towards afternoon, however, $\Delta\theta$ increases as more stable layers are encountered by the rising mixed layer and therefore Ri increases again.

Figure 6 shows Δh normalized by h, as a function of Ri. Included in the graph are the laboratory data of Deardorff *et al.* (1980). Measurements with clouds present have been excluded. It appears that the atmospheric and laboratory data were taken under a similar range of Richardson number (Ri). Atmospheric measurements for $\mathrm{Ri} < 10$ are entirely due to the last three case studies when neutral layers were present above the mixed layer. The best fit through the observations is given by the curve:

$$\frac{\Delta h}{h} = 0.23 + 1.57\,\mathrm{Ri}^{-1}. \tag{8}$$

Repeating the calculations with divergence included resulted in a best fit of:

$$\frac{\Delta h}{h} = 0.24 + 1.28\,\mathrm{Ri}^{-1}. \tag{9}$$

Both results are close to results from laboratory observations (Deardorff *et al.*, 1980) where:

$$\frac{\Delta h}{h} = 0.21 + 1.31\,\mathrm{Ri}^{-1}. \tag{10}$$

The scatter present in the data of Figure 6 is considerably reduced by plotting the data without normalization (Figure 7). It appears as if the scatter may be related to the wide range of mixed-layer heights observed during collection of the data ($h_{\max}/h_{\min} = 12$ for

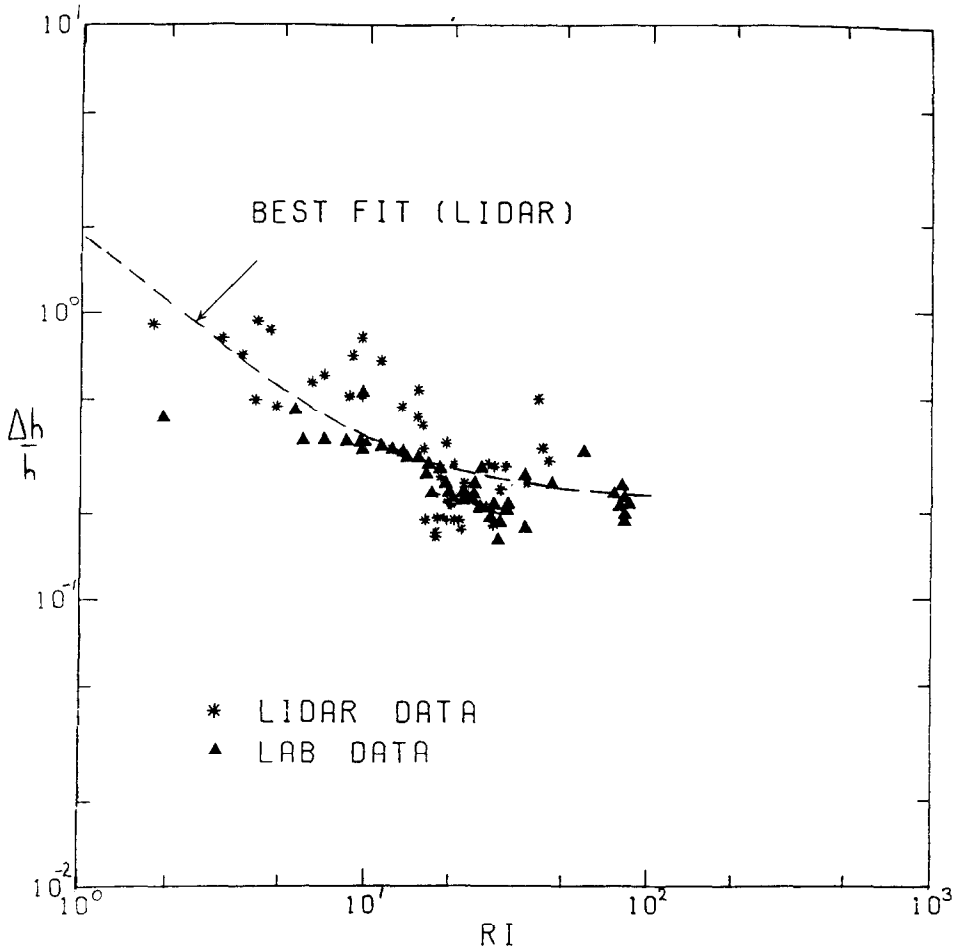

Fig. 6. The normalized thickness of the entrainment zone $\Delta h/h$ versus a convective Richardson number $\mathrm{Ri} = (g/T_0)\,\Delta\theta h/w_*^2$. The lidar data were collected during 6 days of clear-air convection in central Illinois (July 16–21, 1979). The curved line is the best fit through the lidar data which is indicated by *-s, ($\Delta h/h = 0.23 + 1.57\,\mathrm{Ri}^{-1}$). The data have been derived from Table I. Only data gathered under clear conditions are considered. Laboratory data from Deardorff *et al.* (1980) are indicated by triangles.

the atmospheric observations, while $h_{\max}/h_{\min} = 4$ for the laboratory observations). It suggests that the mixed layer height h is not the right scaling parameter to collapse the data onto a single curve. Plotted in log-log form, the data fall closely on a straight line, which is indicative of a power-law dependence,

$$\Delta h = C_1 \left(\frac{T_0}{g\Delta\theta} w_*^2 \right)^{\beta}. \tag{11}$$

We found $\beta = 0.41$, $C_1 = 38.41$, while a value of $\beta = 1$ is expected based on parcel theory. Similar results are obtained when plotting the tank data of Deardorff *et al.* (1980)

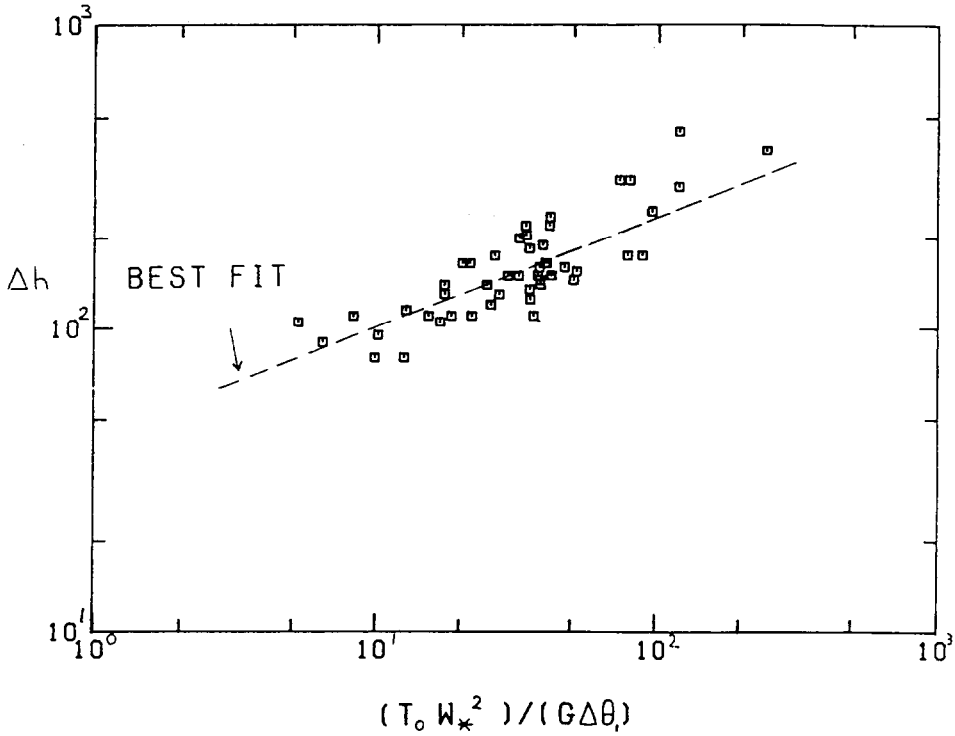

Fig. 7. The thickness of the entrainment zone versus the theoretical prediction $T_0 w_*^2$. Broken line represents the power law. $\Delta h = 38.41\ (T_0 w_*^2 / g\Delta\theta)^{0.41}$

in this form. The poor agreement of both the atmospheric and laboratory data with parcel theory shows that other processes such as entrainment and the induction of gravity waves act to complicate the simple exchange of potential and kinetic energy on which (1) is based. While the precise effect of entrainment remains unclear, its role is to consume energy that otherwise could be used to deepen the entrainment zone; hence the relatively small value of β.

It might be argued that the scaling of kinetic energy on w_* is not appropriate, since our data were not selected under purely convective conditions. A more suitable parameter might be σ_w, where σ_w is a function of w_*, the friction velocity u_* and the wind speed jump Δu across the entrainment zone since both the shear production from the surface and from the top of the mixed layer can be important in determining the overshoot of a plume. In the absence of any mean wind shear, sufficient local velocity gradients can be generated by the upward convective motions at the top of the mixed layer, so that Kelvin–Helmholz instabilities occur and local mixing results. In the presence of large-scale induced wind shear, similar Kelvin–Helmholz instabilities might occur, but the interactions of the two shear mechanisms with the convective motions will obscure their separate influence. In addition, a convective plume moving upward in a shearing environment might be blown over, such as frequently is observed on a

larger scale with developing cumulus clouds. For these reasons, it is not clear whether the effect of shear would be to increase or to decrease the depth of the entrainment zone. It is also not clear how the shear contributions affect the scaling of the kinetic energy. Investigators have proposed that contributions to kinetic energy by u_*, and by the convective velocity scale w_*, be additive (Zeman and Tennekes, 1977) or that their fluxes be additive (Driedonks, 1982). This approach, however, does not recognize that under convective conditions, contributions to the kinetic energy by u_* are likely to have a scaling length of the order of the depth of the surface layer instead of the mixed-layer depth. With this smaller length scale, most of the mechanical turbulence is dissipated before it reaches the top of the mixed layer. This has been verified indirectly by results from the Minnesota experiment, where the dominant scaling velocity inside the bulk part of the mixed layer was w_*, while at the same time u_* was far from small (0.2–0.4 m s^{-1}) (Kaimal *et al.*, 1976). Attempts were made to identify clusters of points on Figure 6 for which the ratio h/L (where L is the Monin–Obukhov length) was large, or for which ΔU was large. In both cases, the clusters were generally associated with the larger Ri-values but did not depart significantly from the curve through the data. Because of the lack of any suitable theoretical framework to incorporate the effects of u_* and ΔU, we only reported the values of u_* and ΔU as extra columns in Table I.

Figure 8 presents relation (4) for the present data set. A best fit through the data results in

$$\frac{\Delta h}{h} = 0.09 + 5.50 \frac{1}{w_*} \frac{\mathrm{d}h}{\mathrm{d}t} \tag{12}$$

which is close to the relation which can be derived from the laboratory experiment:

$$\frac{\Delta h}{h} = 0.19 + 5.35 \frac{1}{w_*} \left(\frac{\mathrm{d}h}{\mathrm{d}t} - \overline{w} \right). \tag{13}$$

Since no data gave values of the normalized entrainment rate of less than 0.02, the asymptotic value of 0.09 is subject to a large standard deviation: 0.03. With divergence included in our calculation, the best fit is:

$$\frac{\Delta h}{h} = 0.005 + 5.75 \frac{1}{w_*} \left(\frac{\mathrm{d}h}{\mathrm{d}t} - \overline{w} \right). \tag{14}$$

These relationships suggest that in the case of no entrainment, Δh would still have a finite value. This could happen under stratified conditions when convection is not strong enough to promote entrainment, e.g., in the early morning or late afternoon. A finite value of Δh would then be maintained by gravity waves riding on the interface. The difference in the asymptotic values between the two experiments is explained by the difference in the range of the nondimensionalized entrainment rate (primarily between 0.02 and 0.05 for our data, and between 0.006 and 0.02 for the laboratory experiment). Therefore, we conclude that only for relatively high entrainment

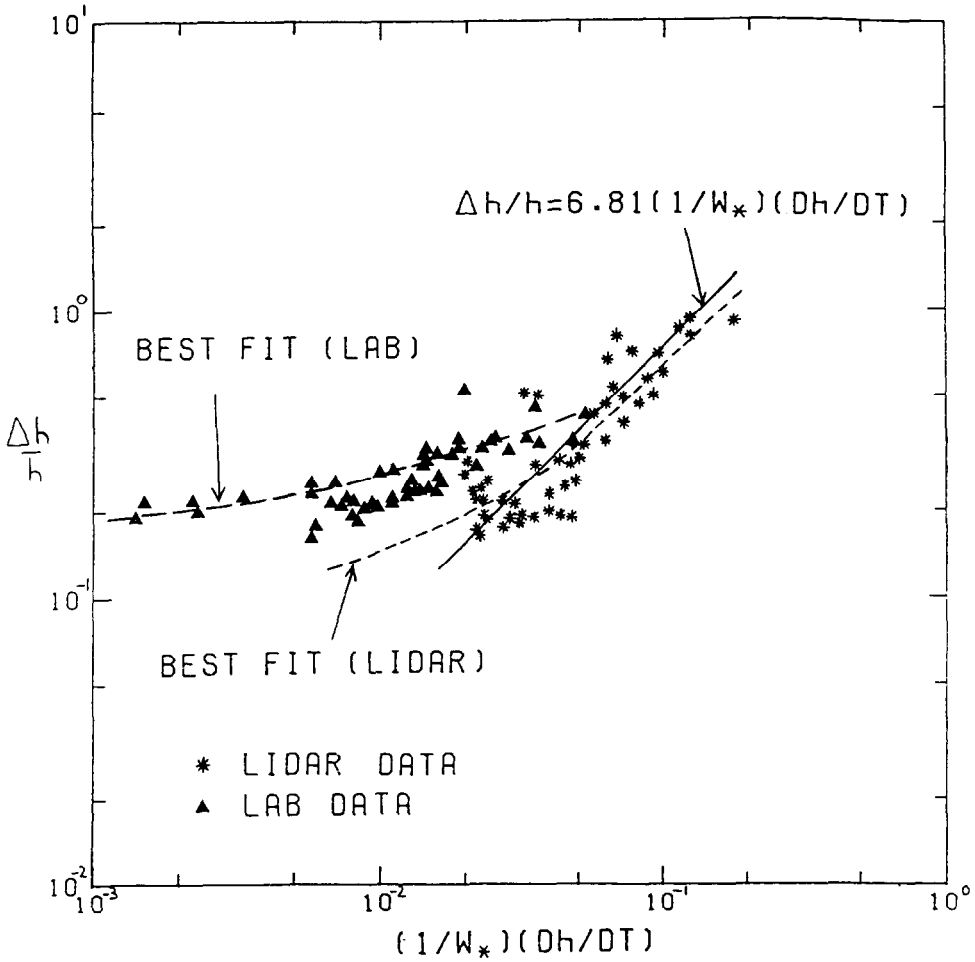

Fig. 8. The normalized thickness of the thickness of the entrainment zone versus normalized entrainment rate, * lidar data, Δ laboratory data. Best fits through lidar and laboratory data are indicated in the graph.

$(1/w_*(\mathrm{d}h/\mathrm{d}t - \overline{w}) > 0.02)$ is Equation (4) satisfied. When the data are fitted using Equation (4), a best fit value of the constant $\alpha = 6.81$ is found.

5. Conclusion

Lidar measurements of the entrainment zone were derived from six case studies of clear-air convection above flat terrain. The mixed-layer height varied between 100 and 1500 m, while the thickness of the entrainment zone varied between 20 and 700 m.

For the purpose of testing theories that predict Δh, we developed a new method to measure the potential temperature jump across the entrainment zone. Agreement with pilot balloon observations was fair.

Predictions of the thickness of the entainment zone based on parcel theory do not agree with the data. Normalizing the entrainment-zone data with the mean mixed-layer height results in a substantial scatter in the data suggesting that the mixed-layer height may not be the proper normalization parameter. Laboratory and lidar data were taken under a similar range of Richardson number values; however, the entrainment rate normalized by w_* was higher for the lidar data.

Since both lidar and laboratory data are consistent in rejecting parcel theory, it suggests that further theoretical studies are needed to parameterize the entrainment-zone depth adequately.

An almost linear dependence was found between the normalized entrainment rate and the normalized thickness of the entrainment zone. The laboratory data, however, indicate that an asymptotic value is reached for $\Delta h/h$ when the entrainment rate is small. Since our data covered only large entrainment rates, the small asymptotic value for $\Delta h/h$ found by fitting a line through the data has only a small significance.

Acknowledgements

The data on surface fluxes and balloon soundings of the mixed layer were collected and analyzed by Drs. M. L. Wesely and R. L. Coulter and their research team at Argonne National Laboratory. Their cooperation is gratefully acknowledged. Thanks go to Mary Ann Wells who typed the manuscript.

This research was sponsored by USAROD grant DAAG29–80–K–0070 and by the U.S. EPA through interagency agreement DW3006–01 to DOE. It has not been subjected to EPA Agency Policy review and therefore does not necessarily reflect the view of the Agency. Final stages of this research were performed while the author was a National Research Council Associate at Goddard Space Flight Center.

References

Boers, R., Eloranta, E. W., and Coulter, R. L.: 1984, 'Lidar Measurements of Boundary Layer Dynamics: Tests of Parametized Models of Mixed-Layer Growth Rate', *J. Clim. Appl. Meteorol.* **23**, 247–266.

Deardorff, J. W.: 1979, 'Prediction of Convective Mixed-Layer Entrainment for Realistic Capping Inversion Structure', *J. Atmos. Sci.* **36**, 424–436.

Deardorff, J. W., Willis, G. E., and Lilly, D. K.: 1969, 'Laboratory Investigation of Non-Steady Penetrative Convection', *J. Fluid. Mech.* **35**, 7–31.

Deardorff, J. W., Willis, G. E., and Stockton, B. M.: 1980, 'Laboratory Studies of the Entrainment of a Convectively Mixed Layer', *J. Fluid Mech.* **100**, 41–64.

Driedonks, A. G. N.: 1982, 'Models and Observations of the Growth of the Atmospheric Boundary Layer', *Boundary-Layer Meteorol.* **23**, 283–306.

Hardy, K. R. and Ottersten, H.: 1969, 'Radar Investigations of Convective Pattern in the Clear Atmosphere', *J. Atmos. Sci.* **26**, 666–672.

Kaimal, J. C., Wyngaard, J. C., Haugen, D. A., Coté, D. R., Isumi, Y., Caughey, S. J., and Readings, C.: 1976, 'Turbulent Structure of the Convective Boundary Layer', *J. Atmos. Sci.* **33**, 2152–2169.

Konrad, T. G.: 1970, 'The Dynamics of the Convective Processes in Clear Air as Seen by Radar', *J. Atmos. Sci.* **27**, 1138–1147.

Kunkel, K. E., Eloranta, E. W., and Shipley, S. T.: 1977, 'Lidar Observations of the Convective Boundary Layer', *J. Appl. Meteorol.* **16**, 1306–1311.

Mahrt, L.: 1979, 'Penetrative Convection at the Top of a Growing Boundary Layer', *Quart. J. Roy. Meteorol. Soc.* **105**, 969–985.

Phillips, A. M.: 1972, 'The Entrainment Interface', *J. Fluid. Mech.* **51**, 97–118.

Raymond, E. and Readings, C. J.: 1974, 'A Case Study of the Structure and Energetics of an Inversion', *Quart. J. Roy. Meteorol. Soc.* **100**, 221–223.

Sroga, J. T., Eloranta, E. W., and Barber, T.: 1980, 'Lidar Measurements of Wind Velocity Profiles in the Boundary Layer', *J. Appl. Meteorol.* **19**, 598–605.

Stull, R. B.: 1973, 'Inversion Rise Model Based on Penetrative Convection', *J. Atmos. Sci.* **30**, 1092–1099.

Stull, R. B.: 1976, 'Mixed-Layer Depth Model Based on Turbulent Energetics', *J. Atmos. Sci.* **33**, 1268–1278.

Tennekes, H.: 1973, 'A Model for the Dynamics of the Inversion Above a Convective Boundary Layer', *J. Atmos. Sci.* **30**, 558–567.

Zeman, O. and Tennekes, H.: 1977, 'Parameterization of the Turbulent Energy Budget at the Top of the Daytime Atmospheric Boundary Layer', *J. Atmos. Sci.* **34**, 111–123.

Appendix: Parameters of the Atmospheric Entrainment Zone

Table I contains values of parameters of the atmospheric entrainment zone as measured and computed from a combination of lidar, pilot balloon and surface data on June 16, 17, 18, 19, 20, and 21, 1979. The following parameters are listed in Table I.

(a) Time (CDT)
(b) friction velocity u_* (m s^{-1})
(c) wind speed jump Δu (m s^{-1})
(d) convective velocity scale w_* (m s^{-1})
(e) mixed-layer rise rate dh/dt (m s^{-1})
(f) potential temperature jump $\Delta\theta_1$ (K)
(g) potential temperature jump with divergence included in the calculations $\Delta\theta_{1D}$ (K)
(h) potential temperature jump $\Delta\theta_2$ (K)
(i) convective Richardson number Ri_1 (no units)
(j) convective Richardson number Ri_2 (no units)
(k) convective Richardson number Ri (no units)
(l) convective Richardson number Ri_D (no units)
(m) surface divergence β_s ($*10^{-5}$) (s^{-1})
(n) spline-fitted mixed-layer height h (m)
(o) entrainment-zone depth Δh (m)
(p) lower edge of the entrainment zone h_0 (m)
(q) cloud (0 = no cloud, 1 = cloud at mixed-layer top)

TABLE I

Data summary of measurement periods

(a) Time CDT	(b) u_* (m s^{-1})	(c) Δu (m s^{-1})	(d) w_* (m s^{-1})	(e) dh/dt (m s^{-1})	(f) $\Delta\theta_1$ (K)	(g) $\Delta\theta_{1D}$ (K)	(h) $\Delta\theta_2$ (K)	(i) Ri_1	(j) Ri_2	(k) Ri	(l) Ri_D	(m) $\beta_s(*10^{-5})$ (s^{-1})	(n) h (m)	(o) Δh (m)	(p) h_0 (m)	(q) cloud (yes = 1)
16 July, 1979																
8:59	0.36	3.1	0.688	0.0218	–	–	–	–	–	–	–	1.6	211	120	150	0
11:50	0.22	2.6	1.318	0.0950	0.84	0.75	0.29	14.5	4.9	19.4	17.9	1.3	908	225	825	1
12:03	0.24	2.8	1.338	0.0870	0.82	0.75	0.34	14.8	6.3	21.0	19.3	1.1	979	235	900	1
12:34	0.24	2.5	1.399	0.0630	0.98	0.88	0.38	18.5	7.0	25.5	23.7	1.6	1119	165	1100	1
12:47	0.24	2.2	1.439	0.0527	1.09	0.97	0.31	20.0	5.7	25.7	23.6	1.8	1164	105	1095	1
13:12	0.30	1.7	1.637	0.0360	0.97	0.84	0.44	14.5	6.7	21.2	19.4	2.1	1230	210	1115	1
13:24	0.29	1.5	1.633	0.0300	0.94	0.81	0.51	14.4	8.0	22.4	20.4	2.3	1254	250	1150	1
14:27	0.28	–	1.435	−0.0055	0.61	0.41	0.84	12.5	17.5	30.0	25.9	3.3	1301	175	1200	1
15:49	0.36	–	1.300	0.0525	0.46	0.24	0.06	12.1	27.9	40.0	34.2	5.0	1364	175	1250	1
17 July, 1979																
8:29	0.25	1.6	0.717	0.0256	2.16	1.98	0.86	33.6	13.4	47.0	44.2	3.6	245	105	185	0
8:54	0.27	1.3	0.811	0.0383	2.18	1.93	0.96	31.7	13.9	45.6	42.0	3.6	293	90	240	0
9:13	0.28	1.3	0.902	0.0451	2.31	2.03	0.70	31.6	9.6	41.2	37.2	3.7	341	110	300	0
9:25	0.29	1.3	0.984	0.0478	2.38	2.06	0.54	30.0	6.8	36.8	32.8	3.7	374	95	340	0
9:38	0.31	1.4	1.075	0.0500	2.28	1.93	0.47	26.6	5.5	32.1	28.0	3.7	412	115	355	0
9:50	0.31	1.6	1.144	0.0510	2.19	1.83	0.41	24.5	4.6	29.1	25.1	3.7	449	110	420	0
10:03	0.30	2.0	1.198	0.0506	2.04	1.66	0.47	22.6	5.2	27.8	23.6	3.7	488	140	425	0
10:15	0.29	2.3	1.246	0.0488	1.95	1.55	0.61	21.5	6.7	28.2	23.8	3.7	524	110	510	0
10:28	0.33	2.5	1.310	0.0455	1.86	1.45	0.72	19.9	7.7	27.6	23.2	3.6	561	165	535	0
10:40	0.37	2.7	1.365	0.0418	1.88	1.45	0.73	19.5	7.6	27.1	22.6	3.6	593	110	585	0
10:53	0.39	2.7	1.418	0.0377	1.85	1.41	0.63	18.8	6.4	25.2	20.7	3.6	624	140	610	0
11:17	0.41	2.4	1.510	0.0324	1.79	1.31	0.59	17.3	5.6	22.9	18.3	3.5	674	150	635	0
11:30	0.46	2.2	1.582	0.0316	1.69	1.20	0.56	15.4	5.1	20.4	16.0	3.5	698	205	600	0
11:43	0.51	2.0	1.651	0.0324	1.52	1.01	0.62	13.2	5.3	18.5	14.1	3.4	723	190	635	0

Table I (continued)

(a) Time CDT	(b) u_* (m s^{-1})	(c) Δu (m s^{-1})	(d) w_* (m s^{-1})	(e) dh/dt (m s^{-1})	(f) $\Delta\theta_1$ (K)	(g) $\Delta\theta_{1D}$ (K)	(h) $\Delta\theta_2$ (K)	(i) Ri_1	(j) Ri_2	(k) Ri	(l) Ri_D	(m) $\beta_s(*10^{-5})$ (s^{-1})	(n) h (m)	(o) Δh (m)	(p) h_0 (m)	(q) cloud (yes = 1)
11:55	0.48	2.0	1.628	0.0341	1.46	0.94	0.55	13.4	5.1	18.5	13.8	3.4	747	165	650	0
12:08	0.45	2.0	1.578	0.0359	1.38	0.85	0.53	14.0	5.4	19.4	14.1	3.4	775	165	715	0
12:20	0.44	2.0	1.557	0.0367	1.34	0.82	0.41	14.4	4.5	18.9	13.3	3.5	801	150	745	0
12:33	0.47	2.0	1.578	0.0365	1.31	0.78	0.31	14.2	3.5	17.7	11.9	3.6	829	160	785	0
12:45	0.49	2.0	1.598	0.0354	1.26	0.73	0.29	13.8	3.1	16.9	11.1	3.7	855	145	825	0
12:58	0.50	1.9	1.575	0.0340	1.22	0.68	0.25	14.1	2.9	17.0	10.8	3.7	882	155	850	0
13:10	0.50	1.8	1.551	0.0336	1.12	0.58	0.27	13.8	3.3	17.1	10.4	3.8	907	115	865	1
13:23	0.49	1.3	1.507	0.0346	1.04	0.50	0.34	14.0	4.6	18.6	11.4	3.9	933	150	850	1
13:35	0.45	–	1.453	0.0364	1.05	0.51	0.30	15.6	4.5	20.1	12.1	4.0	959	120	910	1
13:48	0.43	–	1.398	0.0378	1.01	0.47	0.28	16.7	4.6	21.3	12.5	4.0	988	120	950	1
14:12	0.46	–	1.368	0.0376	1.08	0.55	0.19	19.6	3.4	23.0	13.4	4.1	1042	165	975	1
14:40	0.43	–	1.343	0.0340	1.07	0.53	0.14	21.4	2.9	24.3	13.5	4.0	1103	195	1015	1
15:05	0.45	–	1.377	0.0338	1.04	0.48	0.24	20.7	4.7	25.4	14.5	3.9	1153	135	1065	1
15:41	0.43	–	1.350	0.0338	1.05	0.50	0.39	23.1	8.5	31.6	19.5	3.9	1227	145	1190	1
15:53	0.41	–	1.307	0.0317	1.16	0.59	0.38	27.8	9.0	36.8	23.4	3.8	1251	140	1200	1
16:07	0.39	–	1.236	0.0281	1.20	–	0.50	32.7	13.6	46.3	–	–	1276	165	1200	1
18 July, 1979																
9:44	0.26	0.7	0.992	0.0612	0.84	0.69	0.31	12.5	4.6	17.1	14.8	3.5	448	175	420	0
9:57	0.28	0.6	1.066	0.0602	0.84	0.70	0.17	12.1	2.5	14.6	12.5	3.4	495	220	425	0
10:09	0.30	0.5	1.134	0.0585	0.74	0.58	0.39	10.1	5.3	15.4	13.2	3.3	538	185	490	0
10:22	0.31	0.4	1.196	0.0562	0.63	0.47	0.58	8.3	7.7	16.0	13.9	3.2	582	110	550	0
10:34	0.32	0.3	1.246	0.0537	0.69	0.53	0.65	9.1	8.5	17.6	15.5	3.0	622	125	600	0
10:47	0.32	0.3	1.305	0.0510	0.75	0.59	0.88	9.5	11.2	20.7	18.6	2.9	663	150	605	0
11:00	0.34	0.3	1.399	0.0484	0.81	0.64	0.90	9.5	10.5	20.0	18.1	2.8	702	135	680	0
11:12	0.35	0.4	1.481	0.0463	0.96	0.79	0.78	10.5	8.6	19.1	17.3	3.0	736	140	685	0
11:25	0.34	0.4	1.495	0.0442	1.12	0.92	0.67	12.6	7.6	20.2	18.1	3.2	771	160	720	0

Table I (continued)

(a) Time CDT	(b) u_* (m s^{-1})	(c) Δu (m s^{-1})	(d) w_* (m s^{-1})	(e) dh/dt (m s^{-1})	(f) $\Delta\theta_1$ (K)	(g) $\Delta\theta_{1D}$ (K)	(h) $\Delta\theta_2$ (K)	(i) Ri_1	(j) Ri_2	(k) Ri	(l) Ri_D	(m) $\beta_s(*10^{-5})$ (s^{-1})	(n) h (m)	(o) Δh (m)	(p) h_0 (m)	(q) cloud (yes = 1)
11:37	0.33	0.4	1.485	0.0423	1.16	0.96	0.63	13.8	7.6	21.4	19.0	3.3	802	150	755	0
11:50	0.33	0.3	1.493	0.0401	1.15	0.94	0.63	14.1	7.7	21.8	19.1	3.5	834	145	805	0
12:09	0.34	–	1.552	0.0367	1.20	0.96	0.58	14.3	6.9	21.2	18.3	3.8	878	235	850	0
12:25	0.34	–	1.526	0.0343	1.19	0.92	0.53	15.2	6.9	22.1	18.6	4.0	912	220	850	0
19 July, 1979																
10:37	0.18	–	1.003	0.0994	0.27	0.25	0.14	4.1	2.2	6.3	6.2	−0.7	467	310	425	0
10:52	0.18	–	1.123	0.1802	0.26	0.26	0.01	3.8	0.2	4.0	4.0	−1.0	567	585	315	1
11:23	0.16	–	1.581	0.3498	0.38	0.38	1.21	6.5	20.6	27.1	27.1	−1.6	1307	190	1400	1
11:29	0.14	–	1.610	0.1457	0.69	0.69	0.95	12.1	16.7	28.8	28.8	−1.7	1395	245	1365	1
11:34	0.13	–	1.614	0.0151	0.94	0.95	0.71	16.7	12.6	29.3	29.5	−1.8	1418	270	1340	1
11:38	0.13	–	1.608	−0.0547	0.85	0.86	0.80	15.2	14.4	29.8	29.8	−1.9	1413	255	1335	1
12:11	0.11	–	1.436	0.2093	1.28	1.31	3.69	30.0	86.0	116.6	117.3	−2.5	1482	770	1140	1
20 July, 1979																
8:59	0.20	1.0	0.616	0.0401	0.86	0.82	0.31	11.2	3.9	15.1	14.3	2.9	149	80	120	0
9:09	0.20	0.5	0.664	0.0477	0.72	0.66	0.34	9.3	4.5	13.8	13.0	2.9	175	80	180	0
9:23	0.21	–	0.740	0.0608	0.59	0.53	0.40	7.8	5.2	13.0	12.2	3.0	221	105	200	0
9:35	0.21	–	0.813	0.0744	0.50	0.43	0.24	6.6	3.1	9.8	9.0	3.1	269	130	220	0
9:40	0.22	–	0.845	0.8087	0.49	0.43	0.19	6.5	2.5	9.0	8.2	3.1	292	200	200	0
10:01	0.19	–	0.968	0.1109	0.25	0.19	0.11	3.6	1.5	5.1	4.4	2.9	413	310	280	0
10:14	0.17	–	1.046	0.1311	0.13	0.08	0.14	2.1	2.1	4.2	3.4	2.9	507	450	335	0
21 July, 1979																
9:18	0.17	–	0.763	0.0477	0.57	0.54	0.45	5.9	4.6	10.5	10.2	1.4	185	130	150	0
9:24	0.17	–	0.791	0.0534	0.52	0.50	0.36	5.6	3.8	9.4	9.1	1.4	203	165	150	0
9:41	0.17	–	0.882	0.0772	0.39	0.34	0.17	4.5	2.0	6.5	6.0	1.4	272	150	200	0
9:52	0.16	–	0.916	0.0653	0.29	0.25	0.00	3.6	0.0	3.6	3.2	1.4	321	175	310	0
9:57	0.15	–	0.918	0.0568	0.23	0.20	0.09	3.0	1.3	4.3	4.0	1.4	339	175	325	0

Table I (concluded)

(a) Time CDT	(b) u_* (m s^{-1})	(c) Δu (m s^{-1})	(d) w_* (m s^{-1})	(e) dh/dt (m s^{-1})	(f) $\Delta\theta_1$ (K)	(g) $\Delta\theta_{1D}$ (K)	(h) $\Delta\theta_2$ (K)	(i) Ri_1	(j) Ri_2	(k) Ri	(l) Ri_D	(m) $\beta_s(*10^{-5})$ (s^{-1})	(n) h (m)	(o) Δh (m)	(p) h_0 (m)	(q) cloud (yes = 1)
10:03	0.14	–	0.919	0.0705	0.17	0.14	0.10	2.4	1.3	3.7	3.3	1.4	360	245	270	0
10:09	0.13	–	0.927	0.1159	0.09	0.06	0.12	1.5	1.7	3.2	2.8	1.3	393	295	270	0
10:14	0.12	–	0.941	0.1672	0.02	0.00	0.09	0.3	1.4	1.7	1.4	1.3	436	390	310	0
10:25	0.12	–	1.047	0.2903	0.06	0.04	0.00	1.2	0.1	1.3	1.0	1.3	586	400	475	1
10:37	0.11	–	1.193	0.3804	0.03	0.03	0.12	0.8	2.2	3.0	2.8	1.3	833	635	600	1
10:50	0.11	–	1.336	0.3253	0.00	0.00	0.59	0.0	12.0	12.0	11.8	1.3	1120	340	1090	1
10:56	0.11	–	1.386	0.2501	0.07	0.07	0.66	1.7	13.7	15.4	15.1	1.3	1224	520	1130	1
11:02	0.12	–	1.423	0.1681	0.27	0.25	0.70	5.7	14.6	20.3	20.1	1.2	1299	400	1180	1
11:28	0.15	–	1.574	0.0204	0.28	0.27	1.74	5.4	32.1	37.5	37.3	1.2	1401	520	1180	1
11:39	0.16	–	1.652	0.0341	0.27	0.25	1.99	4.6	33.8	38.4	38.0	1.1	1419	515	1185	1
12:22	0.11	–	1.660	0.0698	0.44	0.42	3.04	8.1	56.2	64.3	64.0	1.1	1561	395	1390	1